Light Manipulation and Applications
https://doi.org/10.70401/lma.2026.0008

Supplementary information

Novel non-diffracting beams engineered via localized spatial frequency mapping

Yuqi Zhang, Wanlin Wang, Zhaojin Guo, Yu Zou, Yanke Li, Xinhao Fan, Bingyan Wei, Dandan Wen, Yi Zhang, Jianlin Zhao, Peng Li, Sheng Liu

S1.Influences of Phase Parameters on the Resulting Non-diffracting Beams

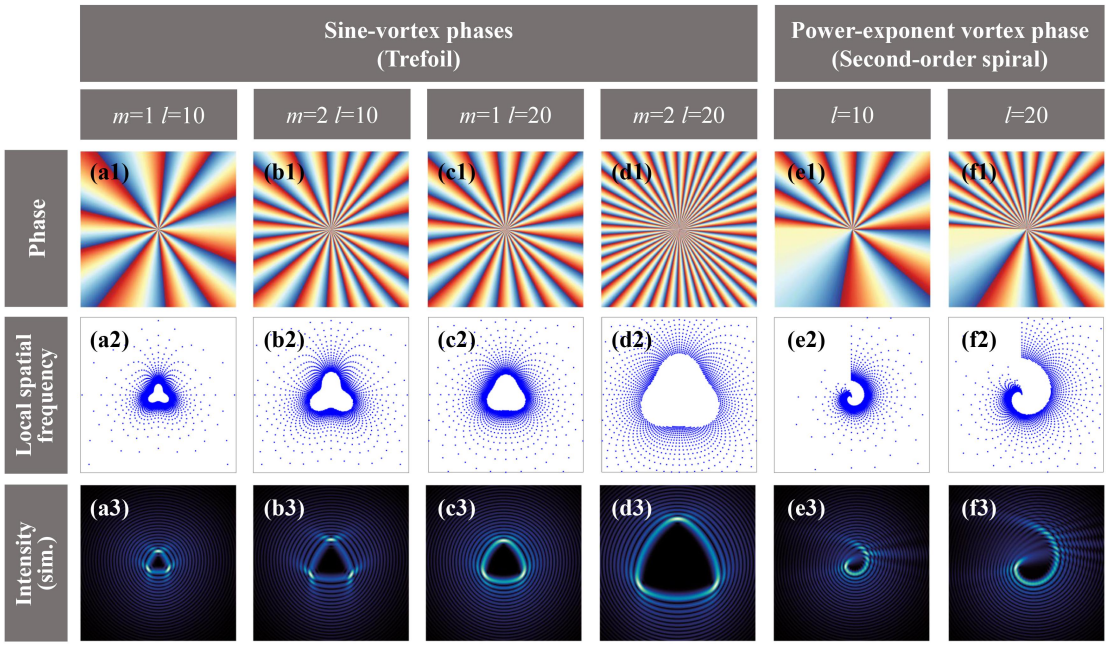

Figure S1. Beam profile modulation via parameters *m* and *l*. Top: Phase distributions; Middle: Spot diagrams of local spatial frequencies; Bottom: Simulated intensity distributions in real space.

In both the sine-vortex phases defined as $\phi_{\mathrm{I}}(r_k, \theta_k) = m[\sin(n\theta_k) + l\theta_k]$, and the power-exponent vortex phase given by $\phi_{\mathrm{II}}(r_k, \theta_k) = 2\pi ml(\theta_k/2\pi)^n$, the parameter *m* acts as a uniform scaling factor that proportionally affect both phase profiles. The impact of this scaling factor on the resulting intensity pattern is demonstrated in Figure S1. For a fixed $n = 3$, panels (a1) to (d1) display the phase distributions of the sine-vortex phases under different combinations of *m* and *l*, with the corresponding local spatial frequency distributions presented in panels (a2) to (d2).

While all local spatial frequency distributions exhibit a trefoil structure, the specific shape and size of the trefoils vary with the parameters. For example, while Figure S1(a2) and S1(b2) share the same *l* value of 10, their *m* values differ (1 and 2, respectively). The higher *m* value corresponds to a greater topological charge (10 vs. 20), producing a similarly shaped but larger trefoil. Furthermore, a comparison between Figure S1(b2) and (c2) shows that they have the same topological charge of 20 yet exhibit slight morphological differences.

It is evident that under sine-vortex phases conditions, proportional scaling of the beam shape cannot be achieved using the single parameter *l* alone. Instead, an additional scaling factor *m* must be introduced to regulate the scaling behavior. A comparison between Figure S1(c2) and (d2) further clarifies the role of m in proportionally amplifying the phase profile.

The corresponding intensity distributions under different parameter settings are presented in Figure S1(a3)-(d3). For the case of n = 2, the power-exponent vortex phase profiles under different values of m and l are shown in Figure S1(e1)-(f1), while the corresponding local spatial frequency distributions are illustrated in Figure S1(e2)-(f2). Comparative analysis reveals that scaling the structural shape via either parameter l or scaling factor m has only a negligible influence on the morphology of the final intensity distribution, as shown in Figure S1(e3)-(f3).

S2.Tailoring Process of the Structured Complex Non-diffracting Beams

S2.1 Tai Chi-shaped Profile

First, let's examine the generation method of the Tai Chi-shaped non-diffracting beam. The ϕ_{total} is defined piecewise as follows:

$$
\begin{aligned}
\varphi_{\text{total}} &= \arg\left[\sum_{j=1}^{3}\exp\left(\mathrm{i}\varphi_j\right)\right] \\
\varphi_1 &= 40\theta_k \\
\varphi_2 &= \begin{cases} 20\theta_k - \dfrac{3k_x}{4}, & 0 < \theta_k \le \dfrac{\pi}{2}, \dfrac{3\pi}{2} < \theta_k \le 2\pi \\ 0, & \dfrac{\pi}{2} < \theta_k \le \dfrac{3\pi}{2} \end{cases} \\
\varphi_3 &= \begin{cases} 20\theta_k + \dfrac{3k_x}{4}, & \dfrac{\pi}{2} < \theta_k \le \dfrac{3\pi}{2} \\ 0, & 0 < \theta_k \le \dfrac{\pi}{2}, \dfrac{3\pi}{2} < \theta_k \le 2\pi \end{cases}
\end{aligned}
\tag{S1}
$$

The outer circular boundary of the Tai Chi-shaped pattern is formed by a sine-vortex phases with topological charge l = 40 and n = 0. The phase distribution, local spatial frequencies, and intensity profile of this outer annular region are presented in Figure S2(a1), (a2), and (a3), respectively. The two central semicircular regions are constructed using circular diffraction-free beams, each carrying a topological charge of l = 20.

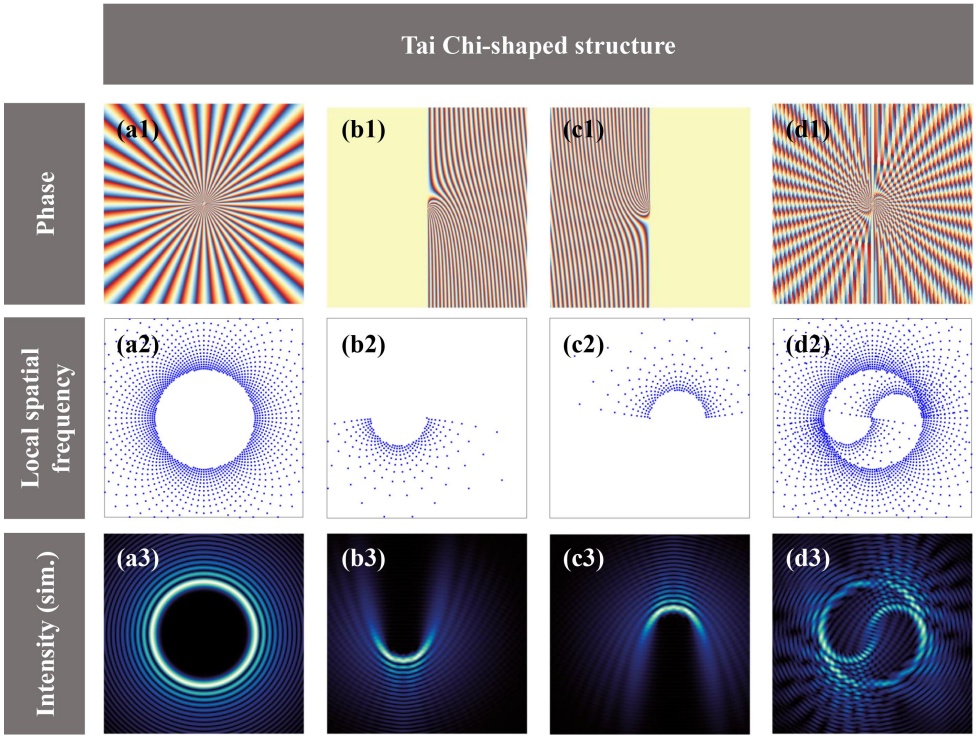

Figure S2. Generation of a Tai Chi-Shaped non-diffracting beam. (a-c) Individual beam components; (d) Synthesized beam. From top to bottom: designed phase distributions in Fourier domain, spot diagrams of the local spatial frequencies for the phases, and simulated real-space intensity distributions, respectively.

Specifically, within the angular sectors $\theta_k \in [0, \pi/2] \cup [3\pi/2, 2\pi]$, the phase function is defined as $20\theta_k - 3k_x/4$, while in the complementary sector $\theta_k \in [\pi/2, 3\pi/2]$, it follows $20\theta_k + 3k_x/4$. The corresponding phase distributions, local spatial frequencies, and intensity profiles for these central regions are shown in Figure S2(b1) through (c3). This configuration, which combines phase structures of different topological charges, ultimately produces a Tai Chi-shaped intensity distribution, as demonstrated in Figure S2(d1) to (d3).

S2.2 Gourd-shaped Profile

By extending the methodology used for generating Tai Chi-shaped non-diffracting beams, we present a phase synthesis approach to construct a gourd-shaped non-diffracting beam. The ϕ_{total} is defined piecewise as follows:

$$\varphi_{\text{total}} = \arg\left[\sum_{j=1}^{2} \exp\left(\mathrm{i}\varphi_j\right)\right]$$

$$\varphi_1 = \begin{cases} 30\theta_k + \dfrac{k_y}{4}, & \dfrac{\pi}{6} < \theta_k \le \dfrac{11\pi}{6} \\ 0, & 0 < \theta_k \le \dfrac{\pi}{6}, \dfrac{11\pi}{6} < \theta_k \le 2\pi \end{cases} \tag{S2}$$

$$\varphi_2 = \begin{cases} 30\theta_k + \dfrac{4k_y}{5}, & 0 < \theta_k \le \dfrac{5\pi}{6}, \dfrac{7\pi}{6} < \theta_k \le 2\pi \\ 0, & \dfrac{5\pi}{6} < \theta_k \le \dfrac{7\pi}{6} \end{cases}$$

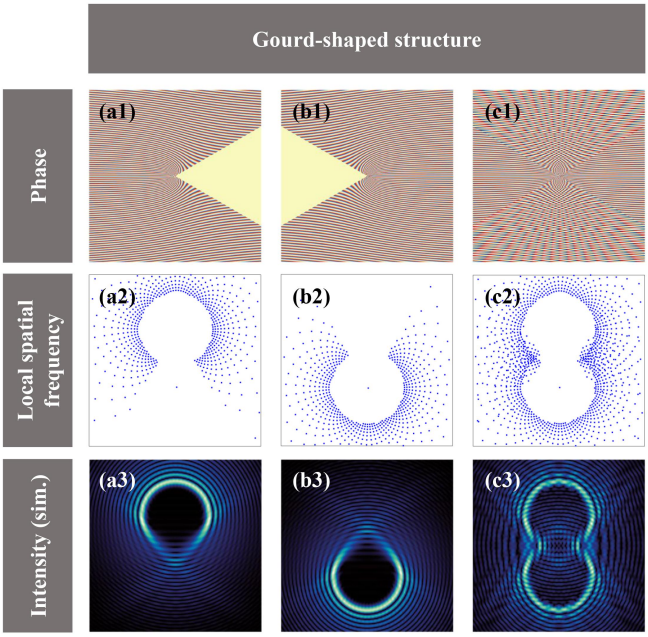

Figure S3. Generation of a gourd-shaped non-diffracting beam. (a, b) Individual beam components; (c) Synthesized beam. From top to bottom: designed phase distributions in Fourier domain, spot diagrams of the local spatial frequencies for the phases, and simulated real-space intensity distributions, respectively.

The phase profile $\phi_1 = 30\ \theta_k + k_y/4$ is defined over the angular domain $\theta_k \in [\pi/6, 11\pi/6]$. The resulting phase distribution, local spatial frequencies, and corresponding intensity profile are illustrated in Figure S3(a1), (a2), and (a3), respectively. The second phase profile, $\phi_2 = 30\ \theta_k + 4k_y/5$, is applied to the complementary angular sectors $\theta_k \in [0, 5\pi/6] \cup [7\pi/6, 2\pi]$, with the segment $\theta_k \in [5\pi/6, 7\pi/6]$ intentionally omitted. The resulting phase map, local spatial frequencies, and intensity distribution for this configuration are presented in Figure S3(b1), (b2), and (b3), respectively.

Since two phase patterns are not complementary, their combination was achieved by superimposing their respective complex amplitude functions and extracting the phase of

the resultant field, as shown in Figure S3(c1). The corresponding local spatial frequencies and real-space intensity distribution of the synthesized phase are presented in Figure S3(c2) and (c3), respectively.

S2.3 Heart-shaped Profile

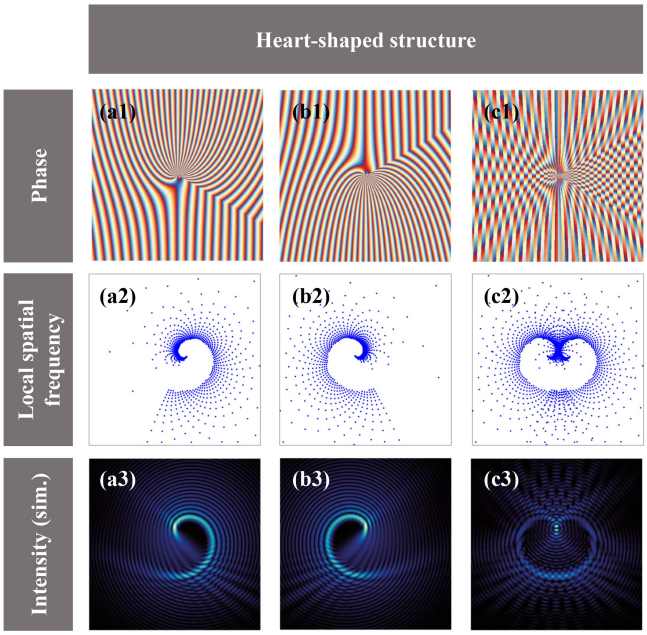

Figure S4. Generation of a heart-shaped non-diffracting beam. (a, b) Individual beam components; (c) Synthesized beam. From top to bottom: designed phase distributions in Fourier domain, spot diagrams of the local spatial frequencies for the phases, and simulated real-space intensity distributions, respectively.

The direct superposition of complete phase profiles (without "cut") can effectively generate non-diffracting optical fields with specific shapes. For instance, a heart-shaped non-diffracting beam can be constructed by superimposing two power-exponent vortex phase. In this design, two power-exponent vortex phase with topological charge l = 20 and nonlinear order n = 2 are adopted, and the total phase distribution is described by the following piecewise function:

$$\varphi_{\text{total}} = \arg\left[\sum_{j=1}^{2}\exp\left(\mathrm{i}\varphi_j\right)\right]$$

$$\varphi_1 = 40\pi\left(\frac{\theta_k - \frac{13\pi}{6}}{2\pi}\right)^2 + \frac{3k_x}{7} \tag{S3}$$

$$\varphi_2 = -40\pi\left(\frac{\theta_k + \frac{\pi}{6}}{2\pi}\right)^2 - \frac{3k_x}{7}$$

The phase distributions, local spatial frequencies, and intensity profiles of the two constituent phases are shown in Figure S4(a1)-(b3). Following rotation and flipping operations applied to these phases and their subsequent superposition, the resulting composite phase ϕ_{total}, together with its corresponding spatial frequency distribution and intensity profile, is presented in Figure S4(c1)-(c3). The final output exhibits a well-defined heart-shaped intensity distribution, demonstrating the feasibility of generating complex optical field configurations through direct phase superposition.

S3.Correlation between Local Spatial Frequency Spot Density and Energy Distribution

In the local spatial frequency spot diagram, the density of the spots reflects the density of energy, meaning that regions with denser spot distributions correspond to higher energy concentrations. As shown in Figure S5, areas with relatively high spot density in the calculated local spatial frequency spot diagram exhibit a good degree of overlap with the bright main lobes in the simulated beam profile.

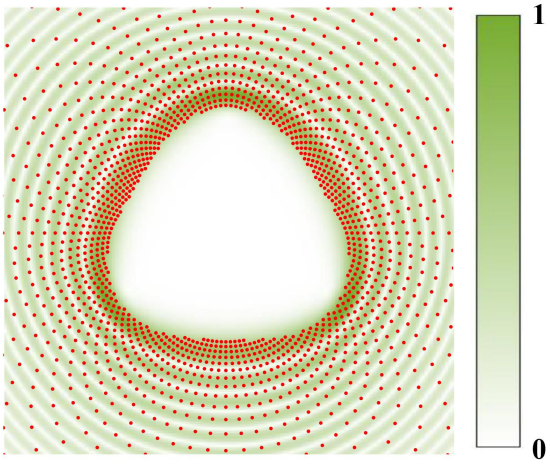

Figure S5. Correspondence between local spatial frequency spot density and real-space intensity distribution.

This trend is similarly evident in the comparison between Fig. 2(a2) (l = 0) and Fig. 2(b2) (l = 30). The spot distribution in the former is more concentrated, corresponding to a more confined energy distribution in real space. In Figs. 2(a3) and (b3), the two intensity profiles are individually normalized in order to better visualize the beam shapes. For further comparison, we performed a unified normalization of the intensity profiles for the trefoil beams with l = 0 and l = 30 , as shown in Figure S6. The results indicate that the overall intensity of the l = 30 beam is relatively lower. This observed trend aligns with the difference in spot density between their respective local spatial frequency spot diagrams (Fig. 2(a2) and (b2)).

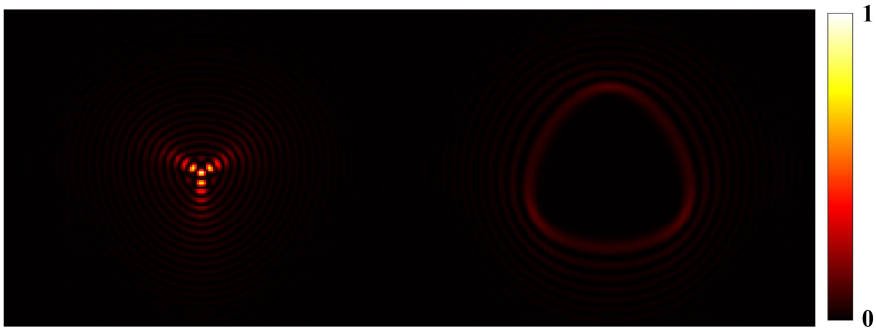

Figure S6. Intensity comparison between trefoil non-diffracting beams with topological charges l = 0 and l = 30

S4.Quantitative Analysis of Self-Healing Experiments

To verify the self-healing capability of the trefoil non-diffracting beam, we employed the Pearson correlation coefficient as a quantitative metric for objectively evaluating the similarity between the beam intensity profiles before and after obstacle obstruction. The Pearson correlation coefficient measures the degree of linear correlation between two variables, with its value ranging from [-1, 1]. A value closer to 1 indicates a stronger positive linear correlation between the two variables. We defined the unobstructed beam intensity profile as variable A and the intensity profile at different propagation distances z after obstruction as variable B. The correlation coefficient between them was calculated using the standard Pearson correlation formula, where $\overline{A}$ represents the mean of A.

$$corr = \frac{\sum_m \sum_n \left(A_{mn} - \overline{A}\right)\left(B_{mn} - \overline{B}\right)}{\sqrt{\left(\sum_m \sum_n \left(A_{mn} - \overline{A}\right)^2\right)\left(\sum_m \sum_n \left(B_{mn} - \overline{B}\right)^2\right)}} \tag{S4}$$

As shown in Figure S7, with increasing propagation distance z, the correlation coefficient rises significantly from 0.412 immediately behind the obstruction (z = 0 cm) to 0.858 at z = 10 cm. This increasing trend indicates that the beam profile gradually approaches its original unobstructed state during propagation. Typically, a correlation coefficient exceeding 0.8 is considered indicative of a strong correlation between two variables. Therefore, reaching a coefficient of 0.858 after 10 cm of propagation demonstrates that the trefoil non-diffracting beam has achieved reasonably good self-recovery.

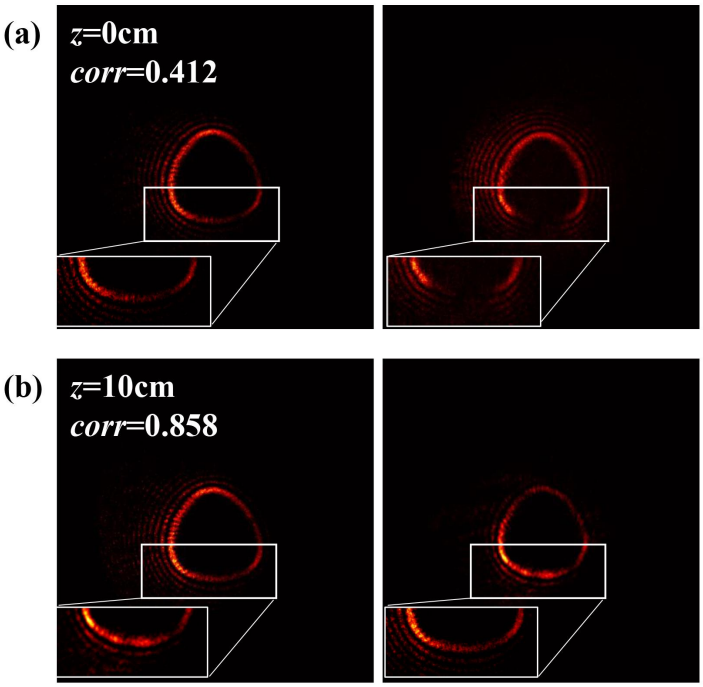

Figure S7. Correlation analysis of intensity profiles in trefoil non-diffracting beam self-healing experiments.

S5.Self-Healing of Tai Chi-Shaped Non-Diffracting Beam

To investigate the universality of the self-healing property in complex-structured beams and to further explore the influence of complex-amplitude interference superposition on self-healing behavior, we supplemented the study with simulation-based verification using a Tai Chi-shaped non-diffracting beam as the subject. This beam is synthesized through the coherent superposition of multiple complex amplitudes, resulting in a wavefront structure that is more intricate than that produced by single-phase modulation.

To verify the self-healing property under conditions closer to the experiment, we simulated three obstruction scenarios with a square-shaped obstacle (size: 234 μm ×234 μm, blocking approximately 1.83% of the beam area) placed at different locations along the propagation path (corresponding to Figure S8(b)–(d)). The recovery process was quantitatively evaluated by calculating the Pearson correlation coefficient between the intensity profiles of the obstructed beam at various propagation distances and those of the unobstructed reference beam (at corresponding positions in Figure S8(a)). The simulation results indicate that at a propagation distance of z = 5 cm, the correlation coefficients for all three cases exceed 0.7, showing preliminary recovery of the main beam structure. Upon further propagation to z = 10 cm, the correlation coefficients reach above 0.98, confirming that the beam intensity profile has become highly consistent with the original unobstructed state, thereby demonstrating effective self-healing. The results show that even under the complex phase

background generated by interference superposition, the Tai Chi-shaped beam still exhibits good self-healing capability. This further indicates that the self-healing property of beams generated through the local spatial frequency mapping and phase-splicing method proposed in this paper possesses a certain degree of universality, and that this property remains preserved even within the complex wavefronts formed by complex-amplitude interference.

Figure S8. Propagation and self-healing of the Tai Chi-shaped non-diffracting beam. (a) Non-diffracting propagation; (b–d) Self-healing of the beam when the obstacle is placed at different positions.

S6.Comparison of Self-Healing Between Bessel and Trefoil Non-Diffracting Beams

For a systematic comparison of the self-healing performance of beams with different structures, we selected a 30th-order Bessel beam and a trefoil non-diffracting beam with the same transverse wavenumber (k_r = 2.564 × 10^4m^{-1}) as the subjects of study.

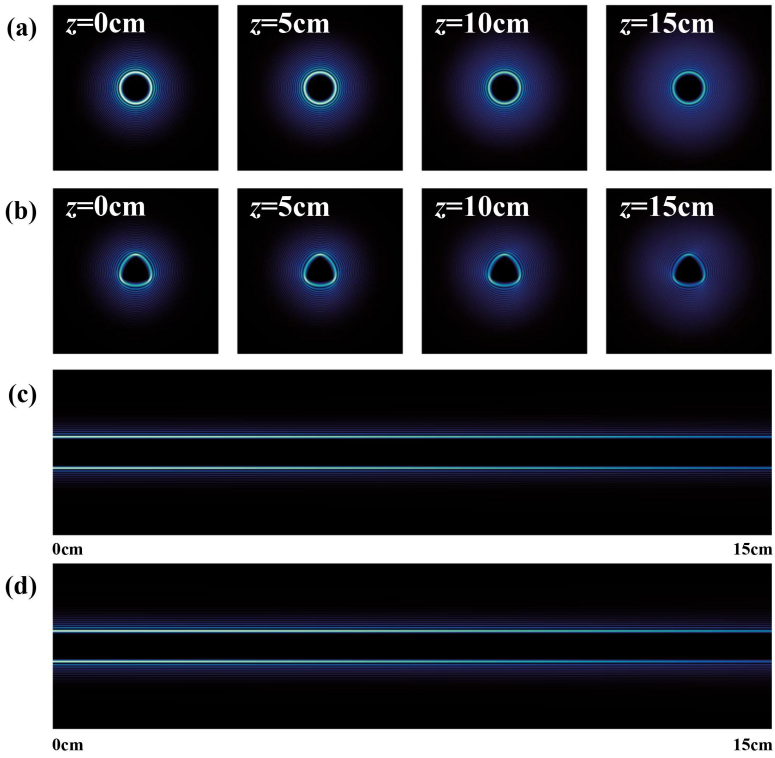

Figure S9. Propagation of a l = 30 Bessel beam and a trefoil non-diffracting beam. (a, c) Bessel beam; (b, d) trefoil non-diffracting beam.

First, under unobstructed conditions, both beams exhibited good propagation invariance over a distance of 15 cm (see Figure S10). Subsequently, a square obstacle (size: 234 μm × 234 μm) was placed at the starting plane of the beam (z = 0cm) to partially block each beam, and the subsequent evolution of their intensity profiles was recorded.

The recovery process was quantified by calculating the Pearson correlation coefficient between the obstructed beam and the unobstructed reference beam at the same propagation position. As shown in Figs. S10(a) and (b), immediately after obstruction the correlation coefficients for both beams dropped below 0.5. With increasing propagation distance, the coefficients rose steadily and reached approximately 0.998 at z = 15 cm. Figure S10(c) illustrates the self-healing process under an increased obstacle size (468 μm × 624 μm). The larger obstruction leads to more severe initial blockage, and at z = 0cm the Pearson correlation coefficient between the beam profile and the unobstructed reference drops to -0.062. As the propagation distance increases, the correlation coefficient continues to rise. Because of the larger blocked area, the propagation distance required to reach the same correlation level is longer than that in Fig. S10(b). Nevertheless, we note that even with the enlarged obstacle, the blocked region largely coincides with the central topological-charge (phase-singularity) region of the beam, rather than fully covering the energy-concentrated main lobe. Consequently, the beam's self-reconstruction process remains effective, and the

correlation coefficient recovers to above 0.96 at z = 10cm, indicating that the intensity profile has become highly consistent with the original state by that point.

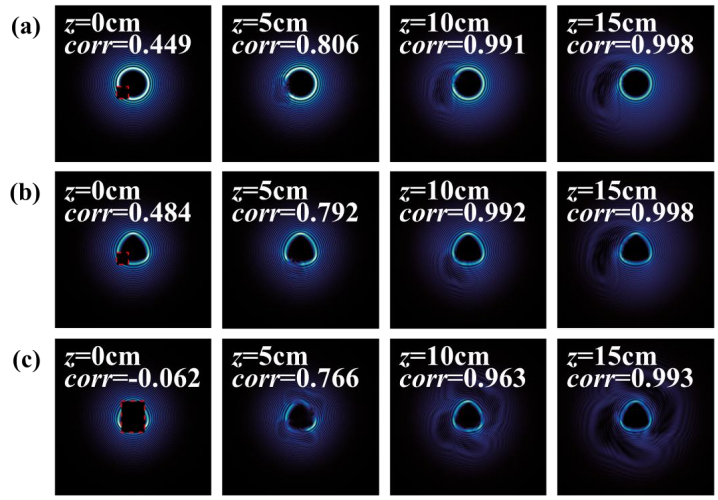

Figure S10. Self-healing of a l = 30 Bessel beam and a trefoil non-diffracting beam. (a) Bessel beam; (b, c) trefoil non-diffracting beam.

To better visualize the relative scale between the obstacle and the beam, we performed simulations using a zeroth-order (l = 0) Bessel beam and a trefoil non-diffracting beam. The unobstructed propagation of both beams over a distance of 15 cm is presented in Figure S11.

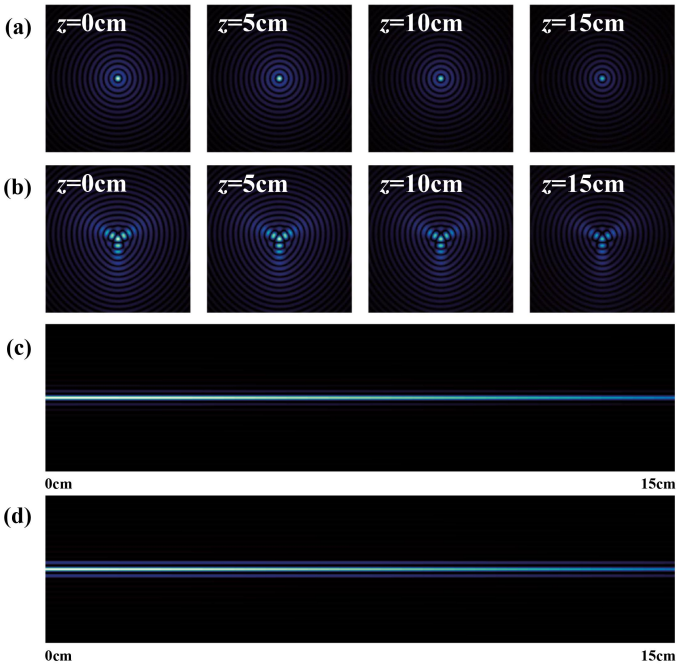

Figure S11. Propagation of a l = 0 Bessel beam and a trefoil non-diffracting beam. (a, c) Bessel beam; (b, d) trefoil non-diffracting beam.

First, a rectangular obstacle measuring 312 μm × 468 μm was used to obstruct the Bessel beam and the trefoil non-diffracting beam (Figs. S12(a, b)). After obstruction, the Pearson correlation coefficients between the intensity profiles of the two beams and their unobstructed reference profiles dropped below 0 at z = 0 cm. As the propagation distance increased, the correlation coefficients gradually recovered. Because this obstacle covered the main energy-concentrated region of the beams, the recovery of both beams was relatively slow, and the correlation coefficients reached only about 0.85 at z = 10 cm.

To examine the influence of obstacle shape on the self-healing process, while keeping the blocked area similar, the obstacle was replaced with a circular one of radius r = 195 μm (Fig. S12(c)). Under circular obstruction, the initial correlation coefficient decreased to -0.011, and the distance required to recover to a level comparable to that of the rectangular case (correlation ≈ 0.85) was 8.5 cm. Compared with the rectangular obstruction (Fig. S12(b)), the recovery was faster, indicating that the obstacle shape affects the self-healing behavior.

Furthermore, the obstacle was fixed as a square (234 μm × 234 μm) and its position was varied to investigate the effect of the blocked region on recovery. In Fig. S12(d), the obstacle was placed at the beam center, obstructing the main lobe. The initial correlation coefficient dropped to 0.052, and about 7 cm of propagation was needed to recover above 0.8. In Fig. S12(e), the obstacle was shifted to a side-lobe region, partially blocking the side lobes while leaving the main lobe largely intact. The initial correlation coefficient here was 0.419, significantly higher than that of the central obstruction, and a high correlation level was reached within a shorter distance (≈5 cm). These results demonstrate that obstruction of the energy-concentrated (main-lobe) region markedly slows down the self-healing process, further revealing the close relationship between the self-healing performance of the beam and both the obstacle location and the energy distribution of the obstructed area.

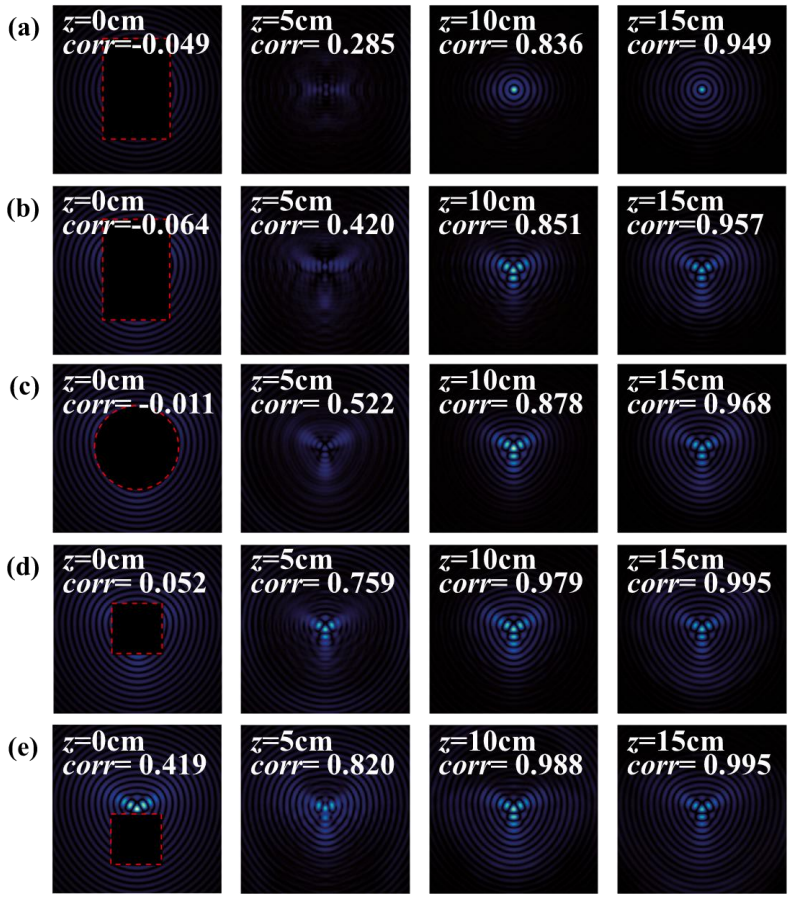

Figure S12. Self-healing of a l = 0 Bessel beam and a trefoil non-diffracting beam. (a) Bessel beam; (b-e) trefoil non-diffracting beam.

Under the various obstruction scenarios described above, the global correlation curves presented in Figure S13 clearly illustrate the differences in recovery dynamics, further confirming the close relationship between self-healing performance and the obstruction area, shape, and energy distribution of the blocked region.

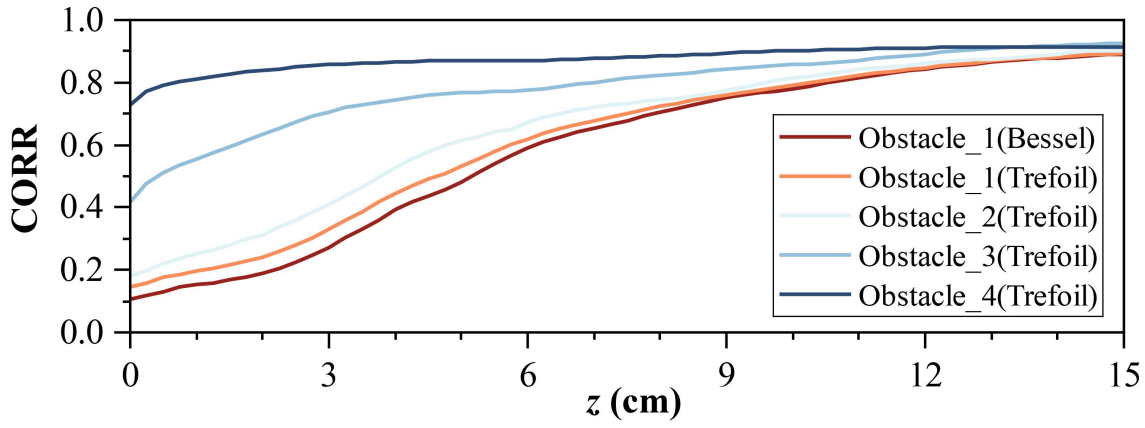

Figure S13. Global correlation curves for the l = 0 Bessel beam and the trefoil non-diffracting beam.

S7.Analysis of Non-Diffracting Propagation Characteristics under Complex Phase Structures

To investigate the influence of more complex phase structures on the non-diffracting properties of beams generated by our method, we performed a series of simulations. First, we designed a multi-aperture phase structure (Figure S14), which better resembles the complex modulation scenarios encountered in practical applications. In the simulation, the transverse wavenumber was set to k_r = 2.564 × 10^4 m^{-1} consistent with the experimental value used earlier. Under ideal conditions (ignoring the limiting effects of system numerical aperture and the cone-angle magnification of the 4*f* setup), the corresponding theoretical maximum non-diffracting range for this k_r is approximately 55 cm. We simulated the full propagation of this multi-aperture non-diffracting beam over this distance.

The results show that the multi-aperture beam maintains good non-diffracting characteristics throughout the 55 cm propagation range. By calculating the Pearson correlation coefficient between the beam profile at the end of propagation (*z* = 55 cm) and its initial profile (*z* = 0 cm), the coefficient remains above 0.9, quantitatively confirming that even with such a complex phase structure, the beam exhibits excellent propagation invariance.

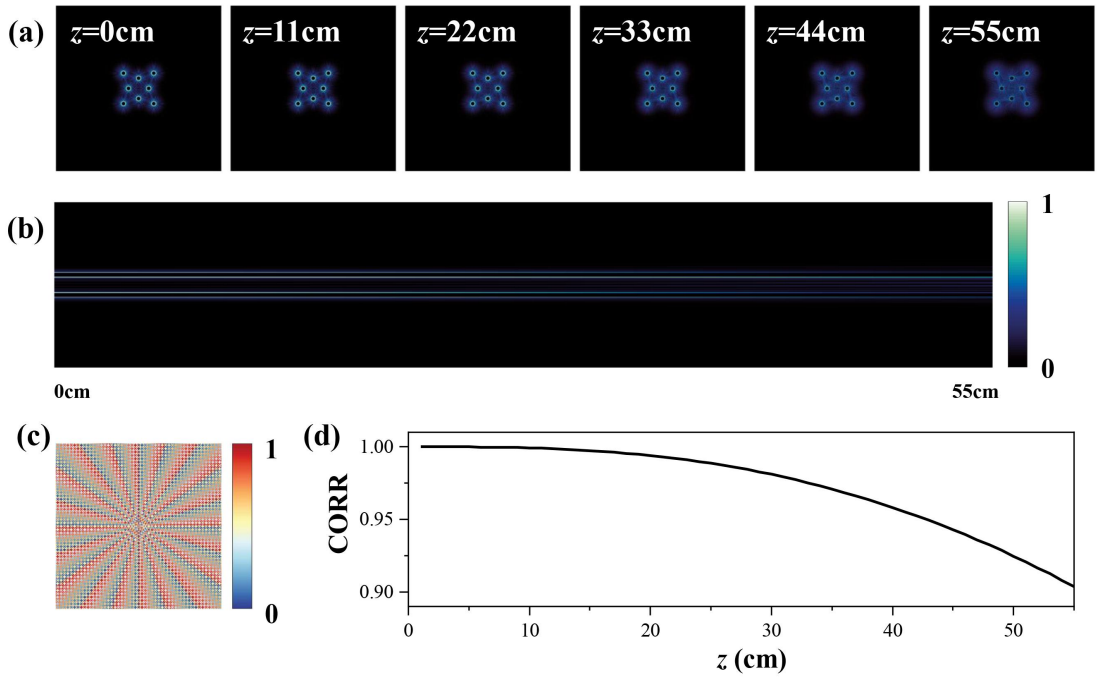

Figure S14. Multi-aperture non-diffracting beam. (a, b) Propagation of the multi-aperture non-diffracting beam; (c) Designed phase distribution in the Fourier domain; (d) Variation of the Pearson correlation coefficient with respect to the initial plane.

Simulations of a flower-shaped non-diffracting beam under the same conditions are shown in Figure S15. The results demonstrate non-diffracting properties comparable to those of the multi-aperture beam, indicating that beams with more intensity inflection points do not experience a significant reduction in their non-diffraction distance.

Subsequently, we performed cutting and splicing on the phase pattern used for generating polygonal beams to create non-diffracting beams in the shape of numerals. As shown in Figure S16, the intensity distribution of the generated beam forms the digits “987” The results demonstrate that the beam exhibits effective splicing and favorable non-diffracting propagation characteristics. However, as the propagation distance approaches the non-diffraction limit, slight interference occurs among the profiles of the three spots. Consequently, when the propagation distance exceeds 54 cm, the Pearson correlation coefficient drops below 0.9.

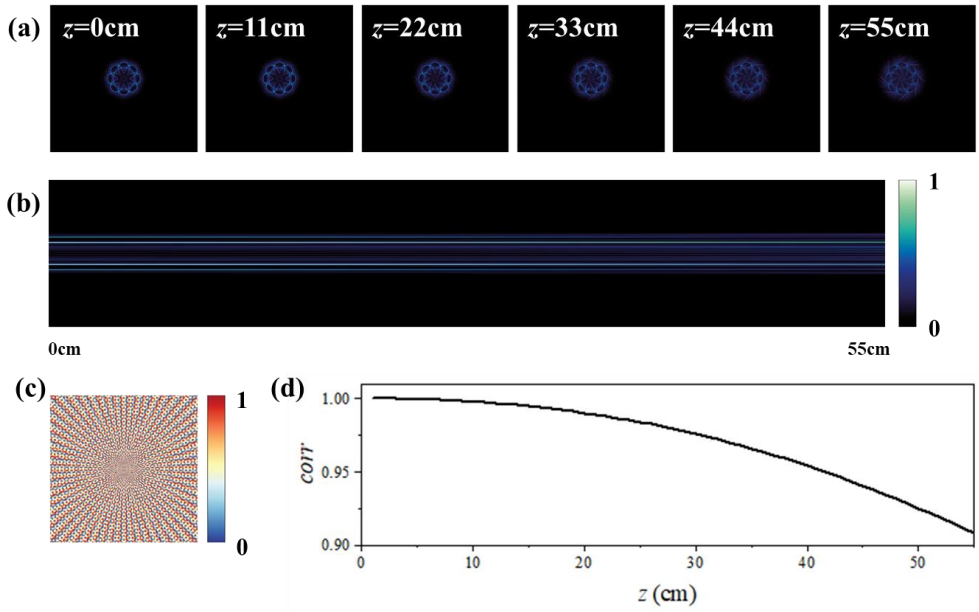

Figure S15. Flower-shaped non-diffracting beam. (a, b) Propagation of the flower-shaped non-diffracting beam; (c) Designed phase distribution in the Fourier domain; (d) Variation of the Pearson correlation coefficient with respect to the initial plane.

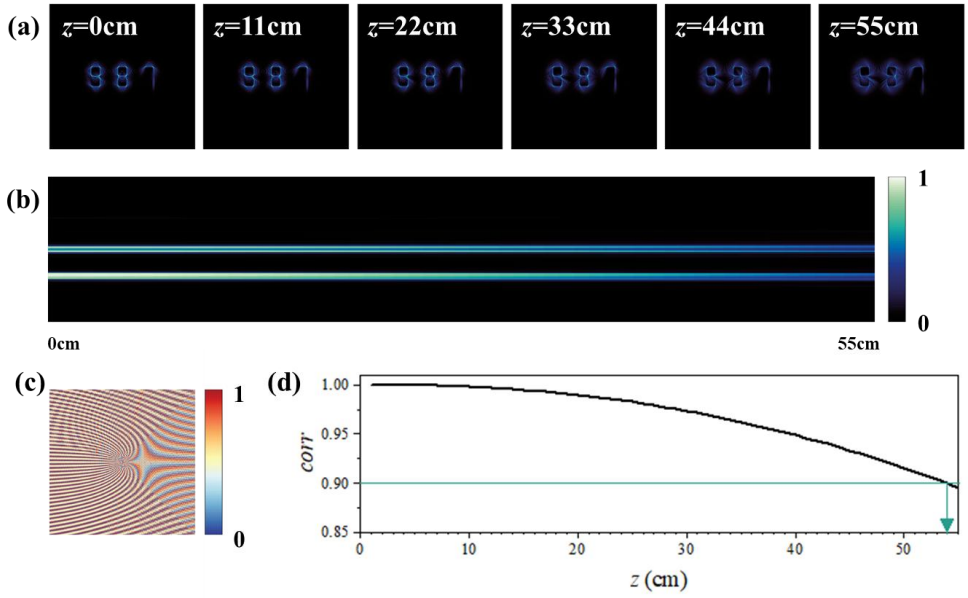

Figure S16. Number-shaped non-diffracting beam. (a, b) Propagation of the number-shaped non-diffracting beam; (c) Designed phase distribution in the Fourier domain; (d) Variation of the Pearson correlation coefficient with respect to the initial plane.

To further increase the phase complexity, we employed a random phase to modulate the annular spectrum. After this modulation, the generated beam no longer exhibits the conventional main-lobe–side-lobe structure in the near field (Figure S17). We simulated the propagation of this random-phase beam over a distance of 55 cm.

The simulation results show that the Pearson correlation coefficient between its profile and the initial plane decreases much more rapidly with propagation distance than for beams with well-defined structures (such as the trefoil or multi-aperture beams). We attribute this primarily to the breakdown of the main-lobe–side-lobe structure, which weakens the beam's self-reconstruction capability during propagation.

Despite this, the random-phase beam still displays a certain degree of propagation stability: its correlation coefficient does not drop below 0.9 until after about 18 cm of propagation. As a control, we simulated the propagation of a Gaussian beam under the same random-phase modulation (Fig.S17(c)); its correlation coefficient falls below the same threshold in less than 1 cm. This comparison demonstrates that even with a highly random, structureless phase, the beam generated by annular-spectrum modulation can achieve a much longer non-diffracting propagation distance than an ordinary Gaussian beam, further confirming the potential of the proposed method for generating non-diffracting beams.

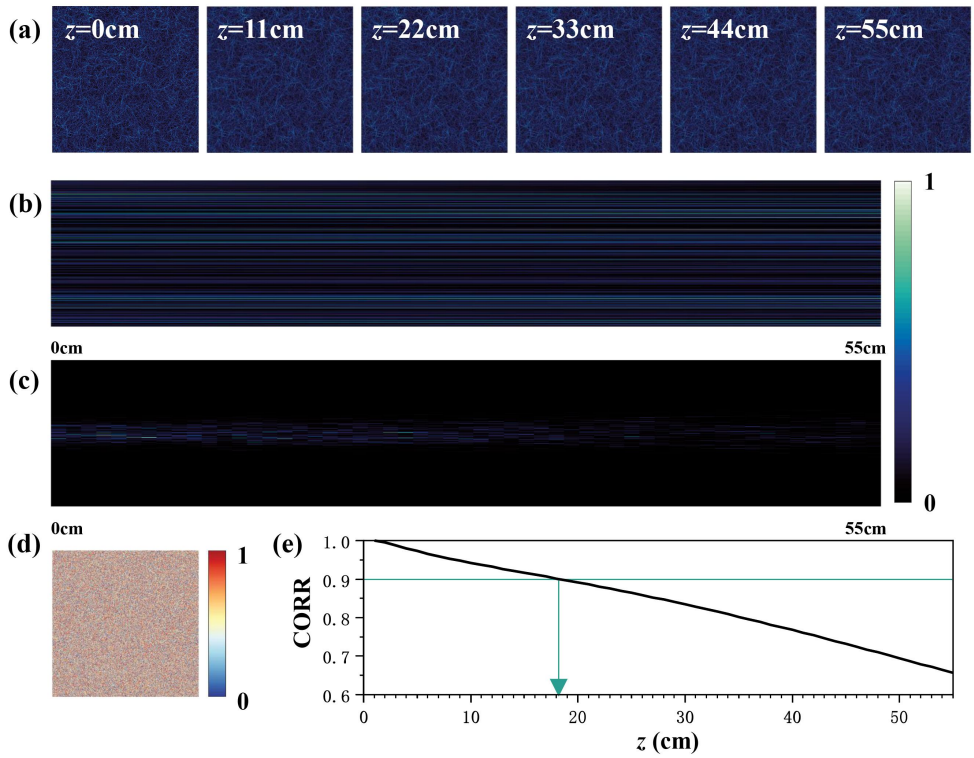

Figure S17. Random-phase beam. (a, b) Propagation of the random-phase beam;(c) Propagation of the random-phase Gaussian beam; (d) Designed phase distribution in the Fourier domain; (e) Variation of the Pearson correlation coefficient with respect to the initial plane.